Aerospace Science and Technology 25 (2013) 273–282

Contents lists available at SciVerse ScienceDirect

Aerospace Science and Technology

www.elsevier.com/locate/aescte

Characterization of the startup and pressure blowdown processes in rocket nozzles

Brian A. Maicke [a,1], Joseph Majdalani [a,*,2], Robert L. Geisler [b,3]

[a] University of Tennessee Space Institute, Tullahoma, TN 37388, United States
[b] Geisler Enterprises, Tehachapi, CA 93561, United States

ARTICLE INFO

Article history:
Received 27 October 2011
Received in revised form 28 January 2012
Accepted 2 February 2012
Available online 8 February 2012

Keywords:
Laval nozzle
Chamber blowdown
Thrust tail-off
Asymptotic approximation
Critical pressure

ABSTRACT

This work is focused on the one-dimensional equations that prescribe the functional modes of a converging–diverging nozzle operating under a range of chamber pressures. Specifically, our study aims at characterizing the flow regimes that are likely to develop inside a Laval nozzle during the blowdown process that takes place at mission's end. Blowdown transients can lead to undesirable sideloads in the nozzle due to flow asymmetries and shock transitions, shock excursions, flow separation, and the formation of recirculatory zones. By representing the flowfield with one-dimensional equations, a direct analytical solution is obtained for the key pressure ratios that control the evolving flow character: supersonic with external shocks, supersonic with optimal expansion, supersonic with internal shocks, or subsonic throughout. These delimiting pressure ratios are determined here using novel asymptotic expansions that enable us to bracket the flow regimes that are particularly susceptible to sideload excursions. The flow attributes of successive flow regimes and their corresponding shock transitions are subsequently explained in view of the pressure evolution that accompanies chamber blowdown. We close with a discussion of experimental observations that suggest the possibility of spin generation during tail-off in the upper stage of a sounding rocket in which slag accumulation is reported.

1. Introduction

Nozzle transients and corresponding flow transitions have long been a source of concern for aerospace engineers. Though often short in duration, transient effects, such as those entailed during the pressure blowdown process, can lead to unpredictable vibrational loads on both the nozzle and vehicle structure. Naturally, the resulting structural vibrations are accompanied by intermittent torques and sideloads that have been repeatedly shown to affect the intended mission profile. For example, sideloads have been observed in a number of hardware configurations including the J2-S [1], Vulcain [18], LE-7A [16,17], and the Space Shuttle Main Engine [8]. In some cases, the severity of sideload transients has been deemed responsible for the damage inflicted on both engine structure and nozzle hardware. Such unsteady motions have also been reported in the development of advanced nozzle concepts, such as the dual bell nozzle [12].

In order to elucidate the physical interactions that evolve during the startup and blowdown processes, it is essential to characterize the flow through a nozzle undergoing variations in the pressure ratio. To this end, the normalized pressure trace of a typical rocket motor is illustrated in Fig. 1 for a) startup and b) blowdown events. For a fully-flowing nozzle at the end of its mission, the nozzle often begins with under-expanded operation (i.e., station ①). Between stations ① and ②, the exit pressure $\bar{p}_e$ remains higher than the atmospheric back pressure, thus ensuring a supersonic discharge out of the nozzle. As the motor completes its burn, the chamber pressure decreases, and the nozzle passes through the first delimiting pressure value at ②; this station denotes an optimal operating condition of a supersonic nozzle with no aftershock effects. In practice, this ideal condition rarely occurs near the end of rocket flight because of inevitable constraints on the mission profile. Instead, it is realized earlier in the mission to prevent the early stages of motor burn from experiencing severe over-expansions.

After crossing the fully-flowing supersonic nozzle pressure ratio, the flow enters the slightly over-expanded regime delineated here as ③. At this stage, oblique shocks begin to form at the edges of the nozzle to the extent that the lower exit pressure will increase to match ambient conditions. These shocks remain external to the nozzle and as such, do not affect vehicle performance. As blowdown progresses, the chamber pressure continues to decline and the flowfield passes through a non-isentropic boundary point,

* Corresponding author.
E-mail address: drmajdalani@gmail.com (J. Majdalani).
[1] Graduate research assistant, Department of Mechanical, Aerospace and Biomedical Engineering.
[2] H.H. Arnold Chair of Excellence in Advanced Propulsion, Department of Mechanical, Aerospace and Biomedical Engineering; Associate Fellow AIAA; Fellow ASME.
[3] Senior rocket scientist.

1270-9638/$ – see front matter
doi:10.1016/j.ast.2012.02.003

Nomenclature

A	local cross sectional area
A_t	nozzle throat area
c_1, c_2	coefficients given by Eq. (32)
p	pressure ratio, $\bar{p}_c/\bar{p}_e$
p_{opt}	normalized exit pressure at optimal expansion station ②, $\bar{p}_{opt}/\bar{p}_e$
p_{sub}	normalized exit pressure at the initial choking station ⑥, $\bar{p}_{sub}/\bar{p}_e$
p_{sup}	normalized exit pressure at station ④ with shock in the exit plane, $\bar{p}_{sup}/\bar{p}_e$
α	first exponent in the isentropic pressure equation, $-2/\gamma$
β	second exponent in the isentropic pressure equation, $-1-1/\gamma$
ε	perturbation parameter, $(A_t/A_e)^2$
γ	ratio of specific heats
ξ	constant related to γ via Eq. (4)

Subscripts and symbols

0, 1	leading and first order
①,②,…	states on the pressure map
c	condition in the chamber
e	condition in the exit plane
n	asymptotic level
t	condition at the nozzle throat
$^-$	condition before a normal shock (minus)
$^+$	condition after a normal shock (plus)
$\bar{}$	overbars denote dimensional quantities

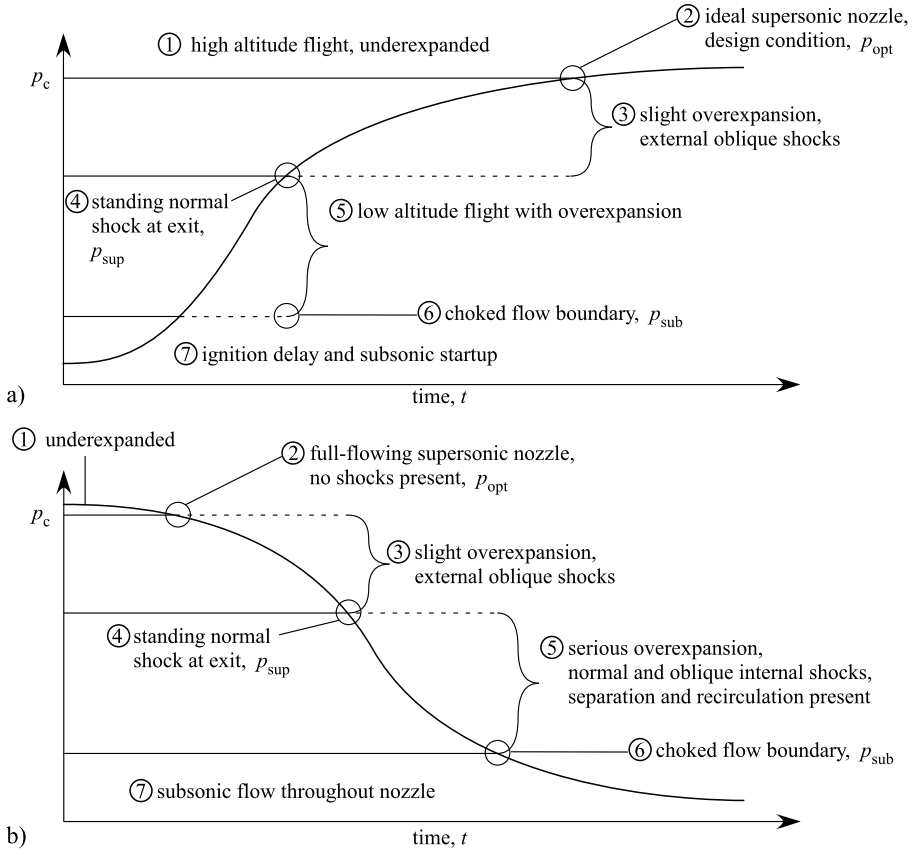

Fig. 1. Pressure trace of a rocket motor during a) startup and b) blowdown.

namely, a standing normal shock in the exit plane, labeled ④ in Figs. 1 and 2.

Further decreases in the chamber pressure give rise to region ⑤ where irreversible processes begin to move into the nozzle as a consequence of both normal and oblique shocks, depending on the nozzle's shape and configuration. In addition to these shocks, flow separation and regions of recirculation are likely to emerge. As these processes unfold asymmetrically, the probability of a resulting net sideload increases. Then as the pressure decreases further, the flow passes through the choking boundary (labeled ⑥ in Figs. 1 and 2). It finally enters the region of fully subsonic flow. In this regime, the flow may no longer remain axial given the absence of supersonic gas expansion in the streamwise direction. At the outset, the three components of the velocity vector become of comparable magnitudes to the extent that tangential velocities and related forces are no longer small relative to their axial counterparts. This is especially true during the evacuation phase of the chamber, which is often accompanied by the formation of bathtub vortices and potential throat area reductions that can be induced by vortex blockage in the nozzle entrance region. At length, as the gaseous mixtures are cooled during the blowdown process, solidification of slag particles can play an increasingly important role in drag generation. The ejection of slag during tail-off can also lead to additional spin transients that are not well understood. In order to theoretically characterize the evolution of these various processes, the pressure blowdown cycle must be carefully tracked inside a traditional, converging–diverging, Laval nozzle.

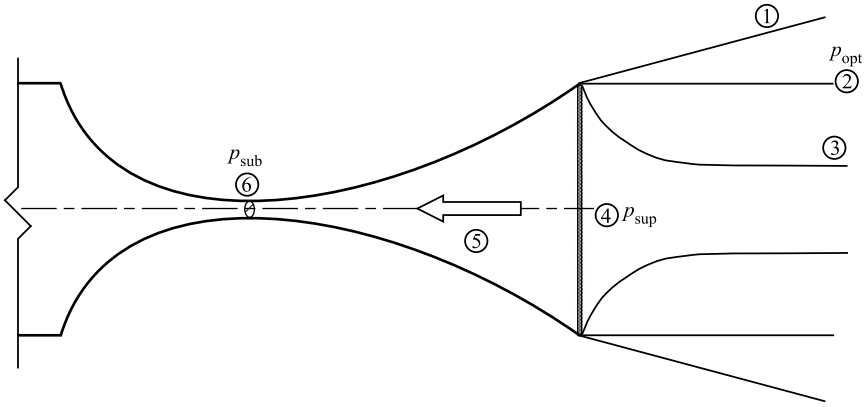

Fig. 2. Various flow configurations depicting regions and threshold states during pressure blowdown.

In actuality, practical applications of Laval nozzles give rise to a set of fundamental challenges to the theoretical analyst. On the one hand, the flowfield may be simple enough to warrant the use of one-dimensional models. On the other hand, even with such an ambitious idealization, the resulting equations are often transcendental to the extent of disallowing direct analytical solutions. Modern textbooks on the subject still include compressible flow tables for handling one-dimensional nozzle expansions. Calculations of vital quantities, such as the nozzle optimal or critical back pressures, are carried out in multiple steps that require either interpolation of tabular data or numerical root finding. In two recent studies, several explicit analytical approximations have been developed for the isentropic thermodynamic relations [11] as well as the area-Mach number equation [10]. These expressions not only augment the existing body of engineering tools, they also enable us to quickly and accurately evaluate fundamental flow properties without resorting to numerical extrapolation or trial. A similar approach based on the Engineering Equation Solver (EES) is elegantly described by Gaggioli [5,6]. Both methods permit the direct implementation of temperature sensitive or spatially varying properties to the extent of improving the precision of reported results.

In its simplest form, one-dimensional, isentropic flow theory offers two roots for the pressure ratio across a Laval nozzle: the subsonic root, which denotes the pressure ratio at which the throat first chokes, and the supersonic root, which corresponds to a fully flowing, supersonic nozzle with shock-free conditions. Between these two pressure ratios, isentropic solutions cannot exist, and a non-isentropic process must be introduced. Evidently, a variety of agents can give rise to entropy increases. For example, both numerical simulations and experiments have shown that viscous effects can initiate oblique shocks, flow separation, recirculation, and expansion waves [4]. Because these effects require a departure from one-dimensional theory, an approximation can be made by introducing a single normal shock at some location within the nozzle.

In hindsight, understanding these critical values may be the key to understanding the effects of transients on nozzle performance. During start-up and shut-down, the pressure in the chamber varies abruptly as the motor cycles up or blows down. While the transient timescales remain short, significant sideloads can be generated during the transition across the over-expanded regime. Though asymmetries in the flow generally drive these sideloads, one-dimensional theory can be faithfully relied on to systematically delineate the boundaries that separate the internal and external shock regions.

In this study, we investigate the ability of one-dimensional nozzle theory to track these dynamically-evolving transition points with an arbitrary level of precision. While this reduced-order model cannot account for multi-dimensional effects, the predominantly axial flow through a supersonic nozzle will be approximated through the use of quasi-one-dimensional expressions, namely Stodola's isentropic area ratio equation and its various derivatives. Here, Stodola's area ratio expression will be combined with the equations for isentropic pressure behavior to retrieve an expression relating the pressure and nozzle area ratio. Additionally, the equation for the pressure jump across a normal shock will be used to directly predict the condition for which a normal shock will occur in the exit plane of a supersonic nozzle. These expressions will be systematically inverted, using formal asymptotic tools, to produce engineering approximations that can pinpoint the transition points directly, without resorting to numerical coding or tabulation.

Before leaving this section, it may be instructive to note that, in describing a multi-dimensional flowfield with a one-dimensional framework, care must be taken to verify the accuracy of the model. In a related study, the authors have compared their one-dimensional isentropic results to a multi-dimensional CFD simulation [10]. The multi-dimensional effects were showcased in the supersonic portion of the nozzle where the computed properties along the centerline and sidewall diverged from their one-dimensional counterparts. Nonetheless, the area-averaged CFD solutions agreed quite consistently with one-dimensional predictions, thus lending support to the nozzle equations considered here.

Evidently, additional features must be investigated in the startup and blowdown phases of a nozzle. Since the flowfield during these transient processes can exhibit strong irreversibilities, the shock relations must be employed where appropriate. The present study constitutes a first step towards a framework that can incorporate non-isentropic effects while retaining an analytical closure for the pressure evolution in a Laval nozzle.

2. Formulation

While the generation of sideloads cannot be handled using a one-dimensional framework, the present model provides a fundamental starting point to separate these more complicated flow regions while retaining analytical closure. The boundaries labeled ② and ⑥ in Fig. 1 are generated using the isentropic pressure relation, reformulated in terms of the area ratio rather than the Mach number. Based on Liepmann and Roshko [9], we have

$$p^{2/\gamma}\left(1-p^{1-1/\gamma}\right)=\varepsilon\left(\frac{\gamma-1}{\gamma+1}\right)\left(\frac{2}{\gamma+1}\right)^{\frac{2}{\gamma-1}} \tag{1}$$

Here ε is the inverse of the expansion ratio squared, p is the pressure ratio $\bar{p}_e/\bar{p}_c$, and γ is the ratio of specific heats. Based on Eq. (1), two branches emerge for a given isentropic expansion. The first denotes the subsonic pressure ratio ⑥ at which the throat

is first choked. The second refers to the supersonic root ② leading to optimal design conditions, with shock-free supersonic flow throughout. From an asymptotic standpoint, two possible routes may be taken: (a) solving for the faster converging ratio and then inverting the final solution so that the chamber pressure appears in the numerator, or (b) inverting the ratio upfront and then solving the modified expression. Results from both methods will be compared in the following sections.

Before addressing the alternate formulations, it may be useful to recall that no isentropic solutions exist between p_{opt} and p_{sub}, or states ② and ⑥ in Fig. 1. The surface of demarcation between externally and internally occurring shocks corresponds to state ④ in the exit nozzle plane where p_{sup} may be calculated using the normal shock relation given by:

$$P = 2\varepsilon\gamma\left[\left(\frac{2}{\gamma+1}\right)\left(1+\frac{\gamma-1}{4\gamma}P\right)\right]^{\frac{\gamma+1}{\gamma-1}}, \quad P = \frac{\bar{p}^+}{\bar{p}^-} \tag{2}$$

In Eq. (2), P represents the pressure change across a shock, with $\bar{p}^+$ being the larger pressure after the shock and $\bar{p}^-$, the smaller pre-shock pressure. This relation may be related to the chamber pressure using the supersonic branch of the isentropic pressure expansion captured by Eq. (1). The equations themselves remain transcendental to the extent of requiring numerical solutions. However, using asymptotic techniques, a set of analytical approximations may be developed for expansion ratios common to most propulsive applications. The solutions may be readily recovered using a recursive form to an arbitrary level of precision. In practice, most propulsive applications only require two terms for a solution with acceptable engineering accuracy (i.e. within 5% of reported measurements).

2.1. Subsonic formulation with regular perturbations

To demonstrate the flexibility of the asymptotic framework, the isentropic equation will be solved for the two different pressure ratio formulations: the faster converging solution with $\bar{p}_c$ in the denominator, and the direct solution with $\bar{p}_c$ in the numerator. First, after some manipulation [11], Eq. (1) may be rewritten as

$$p^\alpha - p^\beta = \varepsilon\xi \tag{3}$$

where $\alpha \equiv 2/\gamma$, $\beta \equiv 1 + 1/\gamma$, and

$$\xi \equiv \frac{\gamma-1}{2}\left(\frac{2}{\gamma+1}\right)^{\frac{\gamma+1}{\gamma-1}} = \frac{\gamma-1}{\gamma+1}\left(\frac{1}{\gamma+1}\right)^{\frac{2}{\gamma-1}} \tag{4}$$

Determining the subsonic root of Eq. (3) requires a regular perturbation expansion which, to arbitrary precision, can be expressed as

$$p = p_0 + \varepsilon p_1 + \varepsilon^2 p_2 + \cdots + \varepsilon^{n-1} p_{n-1} + O\left(\varepsilon^n\right) \tag{5}$$

The resulting form may be substituted into Eq. (3) and then expanded. For the reader's convenience, the expanded equation is presented below at $O(\varepsilon^2)$:

$$\left(p_0^\alpha - p_0^\beta\right) + \varepsilon\left(\alpha p_1 p_0^{\alpha-1} - \beta p_1 p_0^{\beta-1} - \xi\right) + O\left(\varepsilon^2\right) \equiv 0, \quad \forall\varepsilon \tag{6}$$

Because quantities between parentheses must vanish identically for all values of ε, Eq. (6) may be separated into n independent equations that can be sequentially solved for the individual values of p at each order. This operation yields

$$\begin{aligned} p_{sub} = 1 &+ \varepsilon\left(\frac{\xi}{\alpha-\beta}\right) + \varepsilon^2\left[\frac{\xi^2(\alpha+\beta-1)}{2(\alpha-\beta)^2}\right] \\ &+ \varepsilon^3\left[\frac{\xi^3(2\alpha+\beta-1)(\alpha+2\beta-1)}{6(\alpha-\beta)^3}\right] \\ &+ \varepsilon^4\left[\frac{\xi^4(2\alpha+2\beta-1)(\alpha+3\beta-1)(3\alpha+\beta-1)}{24(\alpha-\beta)^4}\right] \\ &+ O\left(\varepsilon^5\right) \end{aligned} \tag{7}$$

The benefit of this representation lies in the solution being applicable to both pressure ratios. By redefining α and β as negative values of the same constants, the solution to the inverted pressure ratio, with the chamber pressure in the numerator, may be readily deduced from the same solution. While the general form of these solutions remains identical, their actual rate of convergence differs. Due to its fractional size, the (smaller) ratio with $\bar{p}_c$ in the denominator converges more rapidly than its converse. Nonetheless, the disparities in convergence remain small and become indiscernible when carried out to $O(\varepsilon^5)$. At the outset, excellent agreement may be expected even with the slower converging approach in which $\bar{p}_c$ appears in the numerator; the latter is taken here as it enables us to solve for the chamber pressure directly.

2.2. Supersonic formulation with undetermined gauges

The supersonic solution may be determined using the Method of Undetermined Gauges. Our starting point is the relation for the new, inverted pressure ratio given by Eq. (3). Through scaling analysis, the leading order is promptly found to be $p_0 = (\varepsilon\xi)^{1/\alpha}$. Then using binomial expansions, Eq. (3) may be transformed into

$$\begin{aligned} &p_0^\alpha\left[1 + \alpha(p_1/p_0) + O(p_1/p_0)^2\right] \\ &\quad - p_0^\beta\left[1 + \beta(p_1/p_0) + O(p_1/p_0)^2\right] - \varepsilon\xi = 0 \end{aligned} \tag{8}$$

Furthermore, when solved for p_1, Eq. (8) returns

$$p_1 = \frac{p_0[p_0^\alpha - p_0^\beta - \varepsilon\xi]}{\beta p_0^\beta - (2/\gamma)p_0^\alpha} \tag{9}$$

Additional terms may be calculated using the recursive relation

$$p_m = \frac{q_m^\alpha - q_m^\beta - \varepsilon\xi}{\beta q_m^{\beta-1} - \alpha q_m^{\alpha-1}}, \quad q_m \equiv \sum_{j=0}^{m-1} p_j \tag{10}$$

The optimal pressure ratio at station ② may hence be deduced by summing all individual contributions, starting with the leading-order approximation. We simply get

$$p_{opt}(\varepsilon, \gamma, n) = p_0 + \sum_{m=1}^{n} p_m \tag{11}$$

The solutions for both branches are provided in Table 1. Compared to the subsonic solution, the inverse problem exhibits a somewhat slower convergence rate when a small number of terms is retained. In practice, the difference between the two approaches becomes insignificant after three terms.

2.3. Shock formulation with flipping and undetermined gauges

The pressure ratio across a normal shock is given by the familiar relation [9]:

$$\begin{aligned} &\frac{p^+}{p^-} = 1 + \frac{2\gamma}{\gamma+1}\left[\left(M^-\right)^2 - 1\right] \\ &\text{or} \quad \left(M^-\right)^2 = \frac{1}{2\gamma}\left[\frac{p^+}{p^-}(\gamma+1) + \gamma - 1\right] \end{aligned} \tag{12}$$

Table 1
Comparison of solutions using $\gamma = 1.6$.

ε	Subsonic, p_{sub}		Supersonic, p_{opt}	
	n		n	
	1	3	1	3
0.05	1.0130	1.0132	58.645	58.764
	1.0128	1.0132	55.840	58.764
0.1	1.0263	1.0270	31.739	31.798
	1.0256	1.0270	29.007	31.796
0.3	1.0834	1.0910	11.355	11.281
	1.0770	1.0906	8.5034	11.250
0.5	1.1472	1.1732	6.7619	6.5728
	1.1283	1.1702	3.6792	6.4902

The pressure ratio p^+/p^- for a normal shock inside a nozzle can be determined as function of the area ratio by substituting the pre-shock Mach number into Stodola's relation, viz.

$$\left(\frac{A}{A_t}\right)^2 = \frac{1}{(M^-)^2}\left\{\frac{2}{\gamma+1}\left[1+\frac{\gamma-1}{2}(M^-)^2\right]\right\}^{\frac{\gamma+1}{\gamma-1}} \tag{13}$$

The resulting expression becomes

$$(\gamma+1)\frac{p^+}{p^-}+\gamma-1 = 2\varepsilon\gamma\left[\left(\frac{2}{\gamma+1}\right)\left\{1+\frac{\gamma-1}{4\gamma}\left[(\gamma+1)\frac{p^+}{p^-}+\gamma-1\right]\right\}\right]^{\frac{\gamma+1}{\gamma-1}} \tag{14}$$

The transcendental nature of Eq. (14) precludes a direct solution. However, using successive approximations, an accurate representation may be achieved. This may be accomplished by first choosing $P = (\gamma+1)p^+/p^- + \gamma - 1$ and then reducing Eq. (14) into

$$P = 2\varepsilon\gamma\left[\left(\frac{2}{\gamma+1}\right)\left(1+\frac{\gamma-1}{4\gamma}P\right)\right]^{\frac{\gamma+1}{\gamma-1}} \tag{15}$$

Eq. (15) can be solved numerically for P. For values typical of nozzle applications, P is found to be a large quantity. This prompts us to introduce $X = 1/P$ and solve for X asymptotically. The X transformed relation becomes

$$X = (\varepsilon\gamma X)^\kappa (aX+b) \tag{16}$$

where

$$a \equiv 4^{\frac{\gamma}{\gamma+1}}\frac{\kappa}{\gamma-1}, \qquad b \equiv 4^{-\frac{1}{\gamma+1}}\frac{\kappa}{\gamma}, \qquad \kappa \equiv \frac{\gamma-1}{\gamma+1} \tag{17}$$

Assuming $X = X_0 + o(X_0)$, one may use the Method of Undetermined Gauges to obtain, at leading order:

$$-(\varepsilon\gamma)^\kappa b X_0^\kappa + X_0 - (\varepsilon\gamma)^\kappa a X_0^{\kappa+1} = 0 \tag{18}$$

Realizing that $X_0 \ll 1$ and $\kappa < 1$, the last term may be ignored, being of higher order. This enables us to balance the first two members of Eq. (18) by setting

$$X_0 - (\varepsilon\gamma)^\kappa b X_0^\kappa = 0 \quad \text{or}$$

$$X_0 = b^{\frac{1}{1-\kappa}}(\varepsilon\gamma)^{\frac{\kappa}{1-\kappa}} = \frac{1}{2}\left[\frac{\gamma-1}{\gamma(\gamma+1)}\right]^{\frac{\gamma+1}{2}}(\varepsilon\gamma)^{\frac{\gamma-1}{2}} \tag{19}$$

Next, we let $X = X_0 + X_1 + o(X_1)$ and expand into

$$X_0 + X_1 - \left[\varepsilon\gamma(X_0+X_1)\right]^\kappa\left[a(X_0+X_1)+b\right] = 0 \tag{20}$$

Factoring out the leading term can be achieved by putting

$$X_0 + X_1 - (\varepsilon\gamma X_0)^\kappa\left(1+\frac{X_1}{X_0}\right)^\kappa (aX_0 + aX_1 + b) = 0 \tag{21}$$

Recalling that $X_1/X_0 \ll 1$, a binomial expansion leaves us with

$$X_0 + X_1 - (\varepsilon\gamma X_0)^\kappa\left[1+\kappa X_0^{-1}X_1 + \frac{\kappa(\kappa-1)}{2}X_0^{-2}X_1^2 + \cdots\right] \times (aX_0 + aX_1 + b) = 0 \tag{22}$$

To expedite matters, we dismiss terms of $O(X_0^{-2}X_1^2)$ that entail negligible contributions. The resulting equation, when solved for X_1, produces

$$X_1 = \frac{(\varepsilon\gamma X_0)^\kappa(aX_0+b) - X_0}{1 - \varepsilon^\kappa X_0^\kappa[a(\kappa+1) + b\kappa X_0^{-1}]} \tag{23}$$

The same technique may be employed to generate higher-order approximations from the following recursive expression,

$$X = X_0 + \sum_{k=1}^{n} X_k, \quad X_k = \frac{(\varepsilon\gamma x_k)^\kappa(ax_k+b) - x_k}{1 - \varepsilon^\kappa x_k^\kappa[a(\kappa+1) + b\kappa x_k^{-1}]}$$
$$x_k \equiv \sum_{j=0}^{k-1} X_j \tag{24}$$

In terms of laboratory coordinates, one may use the direct expression

$$\frac{p^+}{p^-} = \frac{1}{(\gamma+1)X} - \kappa = \frac{1}{\gamma+1}\left[1-\gamma+\left(X_0+\sum_{k=1}^{n}X_k\right)^{-1}\right] \tag{25}$$

In order to compare this result to the other threshold values, it is necessary to relate the solution to the chamber pressure. This can be accomplished by multiplying Eq. (25) with the supersonic expansion relationship previously determined in Eq. (11). We readily obtain

$$p_{sup} = \frac{p^+}{p^-}\frac{p^-}{p_c} = \frac{p^+}{p^-}p_{opt} = \frac{1}{\gamma+1}\left(1-\gamma+\left\{\frac{1}{2}\left[\frac{\gamma-1}{\gamma(\gamma+1)}\right]^{\frac{\gamma+1}{2}}(\varepsilon\gamma)^{\frac{\gamma-1}{2}} + \sum_{k=1}^{n}X_k\right\}^{-1}\right) \times \left\{\left[\varepsilon\left(\frac{\gamma-1}{\gamma+1}\right)\left(\frac{2}{\gamma+1}\right)^{\frac{2}{\gamma-1}}\right]^{\frac{\gamma}{2}} + \sum_{m=1}^{n}p_m\right\} \tag{26}$$

With Eqs. (7), (11), and (26) in hand, the operational modes of a Laval nozzle can be pinpointed as the back pressure is reduced from stagnation to under-expanded conditions.

2.4. Alternate shock formulation with undetermined gauges

For the sake of completeness, the slower converging solution is presented here. The corresponding route follows a similar procedure but does not invoke the $X = 1/P$ variable change. The resulting relation becomes

$$P = 2\varepsilon\gamma\left[\frac{2}{\gamma+1}\left(1+\frac{\gamma-1}{4\gamma}P\right)\right]^{\frac{\gamma+1}{\gamma-1}}$$
$$P = (\gamma+1)\frac{p^+}{p^-} + \gamma - 1 \tag{27}$$

Table 2
Summary of one-dimensional relations for nozzle flow characterization.

Boundary name	Asymptotic approximation
Choking Line ⑥	$p_{\text{sub}} = \dfrac{\bar{p}_{\text{sub}}}{\bar{p}_{\text{e}}} = -\sum_{m=0}^{n} \dfrac{\prod_{j=1}^{m-1}[(m-j)\alpha + j\beta - 1]}{(-1)^{(2m)!} m!(\beta-\alpha)^m}(\varepsilon\xi)^m + O\left(\varepsilon^{n+1}\right)$
Optimal Design ②	$p_{\text{opt}} = \dfrac{\bar{p}_{\text{opt}}}{\bar{p}_{\text{e}}} = \varepsilon\xi + \sum_{m=1}^{n} p_m,$ where $p_m = \dfrac{(\sum_{j=0}^{m-1} p_j)^{2/\gamma} - (\sum_{j=0}^{m-1} p_j)^{(\gamma+1)/\gamma} - \varepsilon\xi}{\dfrac{\gamma+1}{\gamma}(\sum_{j=0}^{m-1} p_j)^{1/\gamma} - \dfrac{2}{\gamma}(\sum_{j=0}^{m-1} p_j)^{2/\gamma-1}}$
Nozzle Shock ④	$p_{\text{sup}} = \dfrac{\bar{p}_{\text{sup}}}{\bar{p}_{\text{e}}} = \dfrac{1}{(\gamma+1)X} - m,$ where $X = X_0 + \sum_{k=1}^{n} X_k$, $X_k = \dfrac{(\varepsilon\gamma x_k)^m (a x_k + b) - x_k}{1 - \varepsilon^m x_k^m [a(m+1) + b m x_k^{-1}]}$, $x_k \equiv \sum_{j=0}^{k-1} X_j$

The leading-order term in Eq. (27) may be determined from a judicious balance of dominant terms; in this case, we extract

$$P_0 = 2\gamma\varepsilon^{\frac{1-\gamma}{2}}\left(\frac{\gamma+1}{\gamma-1}\right)^{\frac{\gamma+1}{2}} \tag{28}$$

The remaining corrections may be calculated using successive approximations. For the first-order equation, we obtain

$$(P_0+P_1)^{\frac{\gamma-1}{\gamma+1}} = (2\varepsilon\gamma)^{\frac{\gamma-1}{\gamma+1}}\left(\frac{2}{\gamma+1}\right)\left[1 + \frac{\gamma-1}{4\gamma}(P_0+P_1)\right] \tag{29}$$

The solution for P_1 can be retrieved using the binomial expansion technique that leads to

$$P_1 = \frac{(2\varepsilon\gamma)^{\frac{\gamma-1}{\gamma+1}}(\frac{2}{\gamma+1}) + (2\varepsilon\gamma)^{\frac{\gamma-1}{\gamma+1}}[\frac{\gamma-1}{2\gamma(\gamma+1)}]P_0 - P_0^{\frac{\gamma-1}{\gamma+1}}}{\frac{\gamma-1}{\gamma+1}P_0^{-\frac{2}{\gamma+1}} - (2\varepsilon\gamma)^{\frac{\gamma-1}{\gamma+1}}[\frac{\gamma-1}{2\gamma(\gamma+1)}]} \tag{30}$$

or

$$P_1 = \left[c_1\left(\frac{2}{\gamma+1}\right) + c_1c_2P_0 - P_0^{\frac{\gamma-1}{\gamma+1}}\right] \times \left(\frac{\gamma-1}{\gamma+1}P_0^{-\frac{2}{\gamma+1}} - c_1c_2\right)^{-1} \tag{31}$$

where

$$c_1 = (2\varepsilon\gamma)^{\frac{\gamma-1}{\gamma+1}} \quad \text{and} \quad c_2 = \frac{\gamma-1}{2\gamma(\gamma+1)} \tag{32}$$

Higher-order terms may be determined from the recursive expression,

$$P_n = \left[c_1\left(\frac{2}{\gamma+1}\right) + c_1c_2\sum_{i=1}^{n-1}P_{i_0} - \left(\sum_{i=1}^{n-1}P_i\right)^{\frac{\gamma-1}{\gamma+1}}\right] \times \left[\frac{\gamma-1}{\gamma+1}\left(\sum_{i=1}^{n-1}P_i\right)^{-\frac{2}{\gamma+1}} - c_1c_2\right]^{-1} \tag{33}$$

With the advent of Eq. (33), a comparison between the inverted and non-inverted formulations may be carried out. The inverted values in this case converge more rapidly as they consist of the solution that employs the smaller ratio of the two.

3. Results and discussion

With the one-dimensional boundary values clearly established, it is possible to evaluate existing performance data with the goal of examining the operating pressure ratios during blowdown. It is also possible to determine the range and duration of the pressure variation through which the profile remains susceptible to sideloads. In this vein, the relations in Table 2 are plotted in Fig. 3 versus the expansion ratio of the nozzle to provide a map of the operating boundaries as the pressure ratio across the nozzle varies. The resulting graph displays the boundary curves that conform to the nozzle map. The regions are labeled consistently with Figs. 1 and 2. Throughout, analytical expressions with either 4 or 5 terms are compared to their numerical counterparts to provide a comprehensive map for the nozzle transition points. Practically, for the high expansion ratios common to most propulsion configurations, a few terms of the present approximations provide sufficient accuracy.

3.1. Nozzle operational modes and chamber pressure

As mentioned above, Fig. 3 enables us to identify different nozzle operating modes over a range of back pressure values. In area ① the nozzle remains under-expanded; expansion fans develop in the exit plane as the relatively higher pressure gas seeks to match ambient conditions. Area ③ introduces external oblique shocks, and one-dimensional theory no longer provides an adequate representation of the flowfield. In area ⑤, shock activities become internal, and the flow undergoes a normal standing shock at some location within the nozzle. Finally, in area ⑦, the flow throughout the nozzle turns subsonic. The unbounded nature of the nozzle shock and optimal expansion curves for small values of ε increase the size of computations in the propulsive range of expansion ratios.

In complementing the data on this graph, we reproduce in Fig. 4 the same nozzle map using the faster converging pressure convention wherein all ratios are referenced to the chamber pressure $\bar{p}_{\text{c}}$. As a result, the unbounded behavior is eliminated, and both pressure and ε are rescaled to a $[0, 1]$ interval. It is interesting to note that the skewed triangular, supersonic-to-subsonic transition region ⑤ appears to be quite sensitive to the area ratio ε. On the one hand, the normal shock zone ⑤ displays an inverse correlation, with the normal shock region increasing at lower and, therefore, more practical values of ε. On the other hand, the oblique shock region ③ maintains a relatively constant size for most expansion ratios, with a circumferential boundary that closely resembles a semi-oval in which large excursions only appear for substantially small or large expansion ratios. In most propulsive applications, the expansion ratios ε fall well below 0.1; as such, they lead to a wide range of exit pressures in region ⑤ for which internal shocks may be initiated. At low values of ε, it is clear from Fig. 4 that the internal shock region extends over a much larger pressure range compared to the external shock region ③. This may explain the increased internal shock activities and separation patterns that can occur inside a nozzle during blowdown.

3.2. Comparison to existing studies

To validate the simplified shock model, we apply our asymptotic solution to a number of case studies in the literature. In the first work (see Hagemann et al. [7]), a truncated ideal nozzle with an area ratio of 20.66 and a parabolic nozzle with an area ratio of 30 are examined. Nitrogen gas with $\gamma = 1.4$ is used in this cold

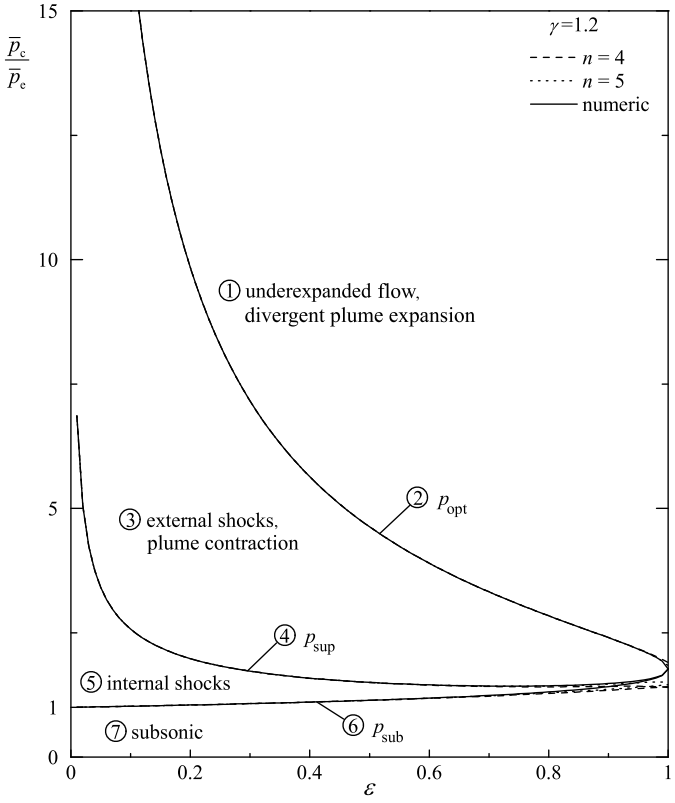

Fig. 3. Pressure map versus ε during chamber blowdown. The vertical axis represents the chamber-to-exit pressure ratio.

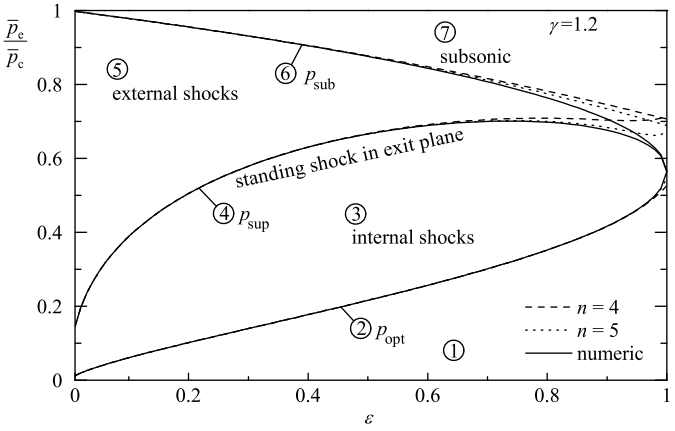

Fig. 4. Inverted pressure map versus ε using the chamber pressure as a benchmark.

flow test configuration. Given the attendant geometric characteristics, one may employ the aforementioned formulation to predict normal shock formation for pressure ratios of $\bar{p}_c/\bar{p}_a = 15.2$ and $\bar{p}_c/\bar{p}_a = 21.7$ using the truncated ideal and parabolic nozzles, respectively.

During startup, the truncated ideal nozzle is reported by Hagemann et al. [7] to sustain a relatively low magnitude sideload with a local peak occurring near a pressure ratio of 5 (see Fig. 5). This value corresponds to our theoretical prediction of the normal shock behavior as ratios below 15.2 can lead to the initiation of strong shocks according to the last entry in Table 2. After the localized peak, the pressure drops precipitously and then slowly recovers back to a maximum value at a pressure ratio of approximately 32. As the pressure decreases during the blowdown process, a similar phenomenon is observed with sideload forces that slowly diminish with the pressure ratio until a localized maximum is reached at a pressure ratio of 5.

Early in the pressure profile, the parabolic nozzle exhibits a similar local maximum: Fig. 5 displays a local peak between a pressure ratio of 7 and 10. This range is justifiable, as the threshold value for the parabolic nozzle is expected to exceed that of the truncated ideal configuration; thus, a delay in the occurrence of sideload peaking seems consistent with theory. The chief dissimilarity between the two contour shapes occurs later in the pressure profile as shown in Fig. 5. Therein, rapid spikes develop near a nozzle pressure ratio (NPR) of 30 and again at 36. These extrema coincide with the transition of the nozzle flowfield from free-shock separation (FSS) to restricted-shock separation (RSS). Free shock separation occurs when the separated flow creates a jet that exits the nozzle undisturbed. In a restricted shock separation, the separated flow reattaches to the nozzle wall, thus generating a recirculation bubble. At the first point (NPR = 30), the flow in the nozzle progresses from FSS to RSS with the recirculation region forming in the nozzle. At the larger pressure ratio of NPR = 36,

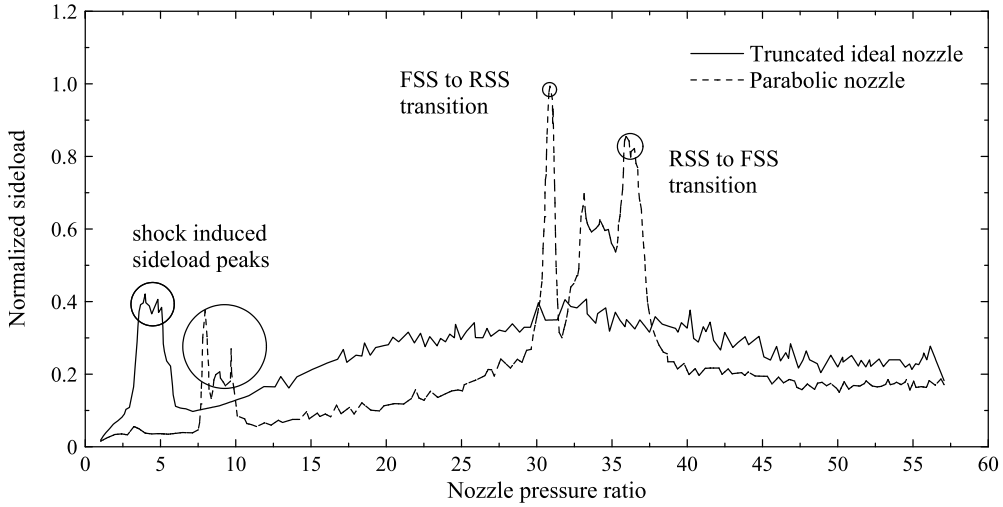

Fig. 5. Normalized sideload during startup versus nozzle pressure ratio based on Hagemann et al. [7]. RSS: Restricted Shock Separation; FSS: Free Shock Separation.

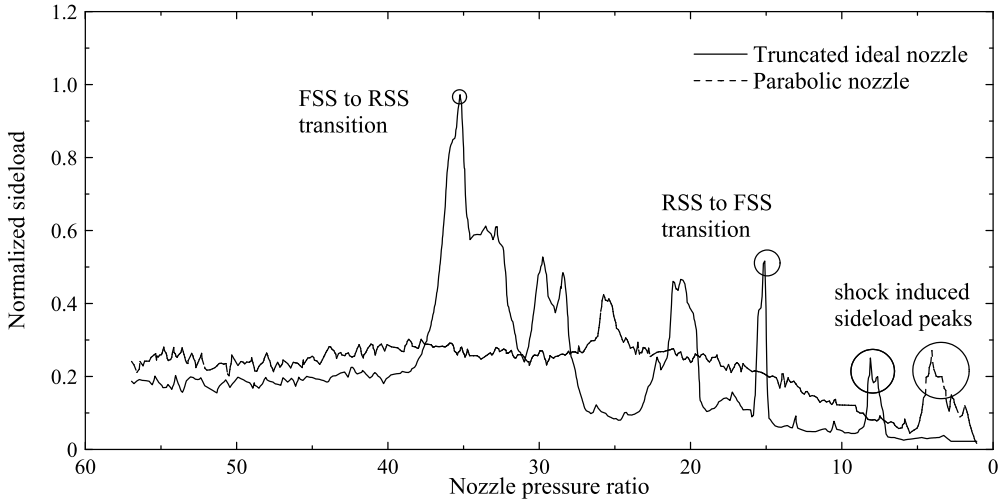

Fig. 6. Normalized sideload during blowdown versus nozzle pressure ratio based on Hagemann et al. [7].

the recirculation region exits the nozzle, thus causing the flow to return to the FSS state.

During blowdown, a similar process is observed, with the first peak appearing at an NPR of 35 (see Fig. 6). In this case, however, the second peak is delayed, and the transition back to FSS does not occur until $\bar{p}_c/\bar{p}_a = 15$ (a value that falls clearly within the range prescribed by the present model). From these values, it may be seen that RSS transitions develop between NPRs of 1.4 and 1.6 times the normal shock pressure ratio predicted by one-dimensional theory.

In separate work, Shimizu et al. [14] conduct a numerical investigation of the RSS transition mechanism and its associated sideloads. Unlike the work by Hagemann et al. [7], this investigation is more concerned with the sensitivity of RSS transition points on the O/F mixture ratio. The ensuing variability in the O/F mixture ratio can be partially accounted for in the present model by changing the specific heat ratio accordingly. In fact, the findings by Hagemann et al. [7] grant us the opportunity to verify the predicted RSS transition point determined from one-dimensional analysis. The geometry for this case is taken to be the truncated perfect nozzle with an area ratio of 52, in which their simulations detect an RSS transition at NPR = 52. Using a specific heat ratio of 1.4, one may use Eq. (33) to calculate $p_{sup} = 36.9$. Dividing the RSS transition NPR by p_{sup} produces a ratio of 1.4, namely, a value that belongs to the range established in the example above. Shimizu et al. [14] further state that varying the oxidizer fuel ratio from 2.8 to 4.1 triggers a shift in the RSS transition point from 35 to 59. By varying the specific heat ratio in the present model and applying the 1.4 multiplier, an RSS transition zone may be readily predicted between 39.9 and 55.3 for $\gamma = 1.1$–1.5. This agreement is satisfying considering the one-dimensional nature of the present study and its independence of three-dimensional aspects of nozzle contouring.

While these preliminary results lead to quick approximations, it is clear that more research into the nature of the RSS transition points is necessary. Despite the useful correlations developed here, the limitations owed to one-dimensionality must be borne in mind. For example, the model cannot predict if RSS transitions will appear, especially in the absence of a strategy to account for local contour changes that drive RSS behavior. Furthermore, the present work treats both truncated ideal and parabolic nozzles examined by Hagemann et al. [7] similarly, despite the lack of RSS transition data for the truncated ideal nozzle case. Refining the model to further account for contour variations would greatly enhance its predictive capability.

3.3. Motor blowdown data and slag accumulation

Before leaving this subject, we consider in passing the flight data obtained for a sounding rocket tested recently. In this par-

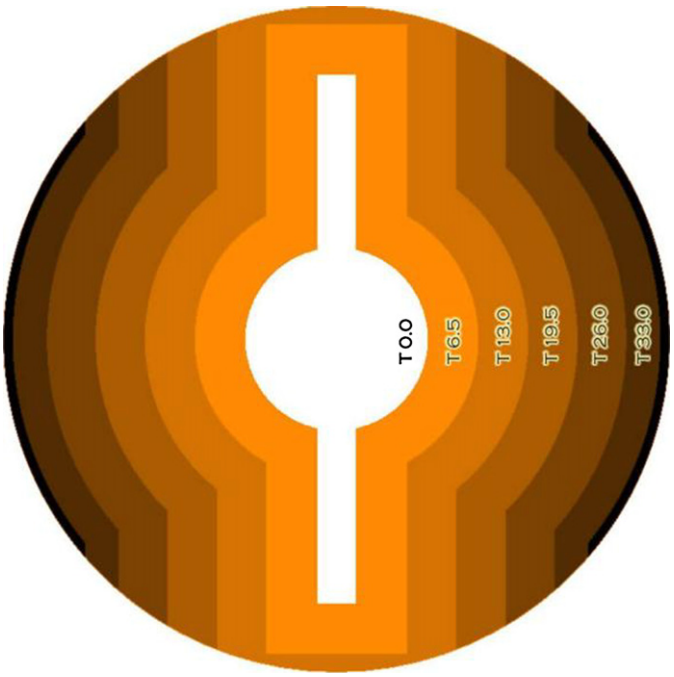

Fig. 7. Grain burnback cross-section versus time (sec) for a sounding rocket upper stage.

ticular case, the formation of nozzle shocks does not constitute the only driving force behind the observed behavior. The sounding rocket test data is therefore presented to simply highlight the additional activities and mechanisms that can accompany pressure blowdown and the need for further refinement of existing theories on the subject.

For this particular sounding rocket motor, flight telemetry shows a significant increase in roll torque as propellant burnback reaches its terminal phase. The motor in question is approximately 43.2 cm in diameter and 533.4 cm in length, including the nozzle. The propellant is aluminized and hence produces a substantial amount of slag during motor burn. The motor itself forms the upper stage of a spin-stabilized sounding rocket. At its nominal operating altitude, aerodynamic drag acting on the stabilizing fins becomes so small that the slightest vortical force on the nozzle inner wall can increase the vehicle spin rate. Furthermore, the grain design comprises two opposed slots as shown in Fig. 7. Based on the burnback cross-sections, it may be seen that two diametrically opposed (black) pools of slag materialize near motor blowdown. These are retained behind the final increment of propellant and appear to be trapped on the case wall due to the centrifugal force exerted by the spinning motor.

The spin rate of the motor and its corresponding pressure trace during tail-off are displayed in Fig. 8 as a function of flight time. The declining motor pressure starts around $t = 31$ sec and triggers a *linear doubling* of roll frequency as the chamber gases blow down. Radar and accelerometer data suggest that a massive expulsion of slag is also initiated simultaneously at 31 sec due to its sudden volumetric expansion from dissolved chamber gases. It is speculated that the slag-laden gas may be swirling at this point to the extent of inducing roll torques that are sufficiently large to cause the vehicle to spin in response to wall friction. Additionally, the sudden accumulation of slag after tail-off may be exacerbated by corner circulation and the drop in both pressure and temperature in the chamber. These factors can promote solidification of the gaseous fraction of aluminum oxide remaining in the chamber.

Pursuant to the strategy described above, we expect two of the threshold values to be of key importance. The first corresponds to the chamber pressure $\bar{p}_{\text{sup}}$ for which a shock may occur in the nozzle exit plane. As in the previous examples, any pressure below $\bar{p}_{\text{sup}}$ can induce shocks within the nozzle. These shocks are prone to spiral around and generate random lateral moments that are accompanied by fluctuations in pitch, yaw, and roll. For the configuration used in this flight test, $p_{\text{sup}} = \bar{p}_{\text{c}}/\bar{p}_{\text{sup}} = 18$, which corresponds to a $\bar{p}_{\text{c}}$ of 45 kPa and an exit pressure of 2.5 kPa. The second threshold pressure corresponds to the minimum chamber pressure $p_{\text{sub}} = 1$ that will still induce choked conditions at the throat. Below this reference value, the flow becomes subsonic throughout. In the process, the supersonic axial velocity magnification in the streamwise direction will cease to occur. The swirling angular momentum becomes of the same order as that of the axial component. For this test, the subsonic pressure ratio approaches unity, which results in an even lower chamber pressure as the test is conducted at high altitude. Furthermore, it may be clearly inferred that internal shock-separation behavior of the type investigated here is not the cause of the increased rotation shortly after burnout. Instead, the rotational effects exhibited must be accounted for in some other manner.

A theoretical explanation of the observed behavior is as follows. When accounting for the effects of a spinning system with variable mass, the spin rate can depend on both the total mass and its spatial distribution. If variations in mass distribution remain slight, it is possible to isolate the effects of mass variability. Mass exiting the vehicle produces an increased spin rate. The growth

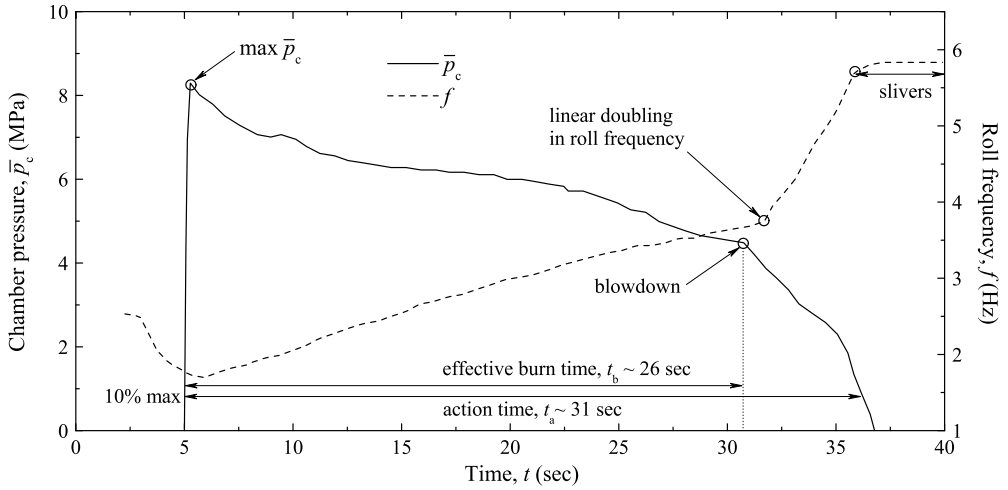

Fig. 8. Grain burnback pressure trace and roll frequency versus time for a sounding rocket upper stage.

normally occurs smoothly, being driven by the constant mass flow rate resulting from choked conditions at the throat. During the slag expulsion event, however, the mass exiting the vehicle increases suddenly. This surge in system mass can induce an increased spin rate on the order of that observed in the flight data.

During normal operation, the high pressure in the motor ensures choking conditions and supersonic expansion in the axial direction. As usual, transonic expansions through the nozzle are dominated by axial motion, thus rendering the effects of the normal (cross-streamwise) and tangential (spin) components negligible. After blowdown, this scenario changes in that, as the pressure diminishes, the axial velocity follows suit. Suddenly, an increase in roll, pitch, and yaw may arise. Such behavior can be attributed to the resurgence of the tangential and normal forces as appreciable contributors. Moreover, a bathtub vortex is typically formed during chamber evacuation, and this causes the spin velocity to increase. From this perspective, the spiraling motion of the slag-laden mixture through the nozzle may be partly responsible for the increase in roll. When the normal and tangential forces are no longer negligible (i.e., when they become of the same relative order as the depreciating axial force), sudden redirections in pitch and yaw may be sensed throughout the motor, in addition to a doubling in roll with the passage of time. As shown in Fig. 8, the sustained doubling in roll frequency occurs shortly after the initiation of pressure blowdown. The linear increase in f continues until the time that marks the beginning of the sliver burnout period. This phase is accompanied by a substantial diminishment in thrust, along with a horizontal flattening in the roll frequency. It is clear from a vehicle dynamics point of view that nozzle transients constitute only a portion of the total contribution to the time-dependent sideloads experienced during flight.

3.4. Other considerations

The present study is not meant to be a comprehensive investigation into blowdown, but rather a first cut towards a simple framework for its modeling and prediction. While the one-dimensional equations treated here provide general breakpoints for nozzle behavior, the limitations of the analysis prevent it from predicting actual sideloads. In practice, experimental investigations have determined that separation inside a nozzle and its associated sideloads are influenced by the local nozzle contour [7]. The present study cannot account for such variations. The asymmetric nature of the separation process causing sideloads requires at least a modified two-dimensional approach to make any sort of prediction possible. In addition, the FSS–RSS transition points exhibit hysteresis when comparing pressurization to blowdown [3,14,15] that the present model cannot accommodate. Finally, it is well known that, in conjunction with steady-state sideloads, oscillatory loads can be experienced during blowdown [2], and these require a time-dependence that the present model lacks.

4. Conclusions

In summary, two threshold pressure ratios are important to note. The first, $\bar{p}_{\text{sup}}$, corresponds to the chamber pressure for which a shock will occur in the nozzle exit plane. Any chamber pressure below this value will trigger shocks inside the nozzle. These shocks can spiral around while producing random lateral moments that induce fluctuations in pitch, yaw, and roll. The next threshold pressure is the minimum chamber pressure, $\bar{p}_{\text{sub}}$, that will still maintain choked conditions at the throat. Below this value, the flow will turn subsonic everywhere, and the supersonic axial acceleration in the streamwise direction will no longer occur. The swirling angular momentum becomes of the same order as that of the axial momentum. In practice, this situation unfolds when the chamber pressure falls under 1.894 (i.e., $1/0.528$) times the outer pressure, thus signaling the onset of subsonic flow throughout the motor.

Today, most nozzle transient predictions are performed using empirical methods that can be refined through engine test correlations, as in the skewed plane method [13], or through numerical simulations [14,15]. An improved analytical framework can help to guide these experimental and numerical investigations, as well as provide insight into the physical processes that affect some of the attendant phenomena. Future research efforts would include incorporation of two-dimensional effects as well as oscillatory models to account for both steady and unsteady forces observed during the blowdown process. It is hoped that these effects will be further investigated, as it seems that they have been habitually avoided in the past.

Acknowledgements

This project was sponsored partly by the National Science Foundation and partly by the University of Tennessee Space Institute.

References

[1] Anon., 4400-Hz vibration investigation, Rocketdyne, Final report R-8742, NAS8-25156, Canoga Park, CA, 1971.
[2] S. Deck, P. Guillen, Numerical simulation of side loads in an ideal truncated nozzle, Journal of Propulsion and Power 18 (2) (2002) 261–269, doi:10.2514/2.5965.
[3] S. Deck, A.T. Nguyen, Unsteady side loads in a thrust-optimized contour nozzle at hysteresis regime, AIAA Journal 42 (9) (2004) 1878–1888, doi:10.2514/1.2425.
[4] M. Frey, G. Hagemann, Restricted shock separation in rocket nozzles, Journal of Propulsion and Power 16 (3) (2000) 478–484, doi:10.2514/2.5593.
[5] R.A. Gaggioli, An alternative (preferable) friction factor, American Society of Mechanical Engineers Paper IMECE2006-13126, Chicago, IL, November 2006.
[6] R.A. Gaggioli, Streamlined modeling of compressible flows, American Society of Mechanical Engineers Paper IMECE2006-13125, Chicago, IL, November 2006.
[7] G. Hagemann, M. Frey, W. Koschel, Appearance of restricted shock separation in rocket nozzles, Journal of Propulsion and Power 18 (3) (2002) 577–584, doi:10.2514/2.5971.
[8] W. Holland, SSME/side loads analysis for flight configuration, NASA Marshall Space Flight Center, Technical report TM-X-6484, Huntsville, AL, 1974.
[9] H.W. Liepmann, A. Roshko, Elements of Gasdynamics, Dover Publications, Inc., 2001.
[10] J. Majdalani, B.A. Maicke, Explicit inversion of Stodola's area-Mach number equation, Journal of Heat Transfer 133 (7) (2011) 071702-7, doi:10.1115/1.4002596.
[11] J. Majdalani, B.A. Maicke, Inversion of the fundamental thermodynamic equations for isentropic nozzle flow analysis, Journal of Engineering for Gas Turbines and Power 134 (3) (2012) 031201-9, doi:10.1115/1.4003963.
[12] E. Martelli, F. Nasuti, M. Onofri, Numerical parametric analysis of dual-bell nozzle flows, AIAA Journal 45 (3) (2007) 640–650.
[13] J. Shi, Rocket engine nozzle side load transient analysis methodology – a practical approach, AIAA Paper 2005-1860, April 2005.
[14] T. Shimizu, H. Miyajima, M. Kodera, Numerical study of restricted shock separation in a compressed truncated perfect nozzle, AIAA Journal 44 (3) (2006) 576–584, doi:10.2514/1.14288.
[15] T.-S. Wang, Transient three-dimensional startup side load analysis of a regeneratively cooled nozzle, Shock Waves 19 (2009) 251–264, doi:10.1007/s00193-009-0201-2.
[16] Y. Watanabe, N. Sakazume, M. Tsuboi, LE-7A engine nozzle problems during the transient operations, AIAA Paper 2002-3841, July 2002.
[17] Y. Watanabe, N. Sakazume, M. Tsuboi, LE-7A engine separation phenomenon differences of the two nozzle configurations, AIAA Paper 2003-4763, Huntsville, AL, July 2003.
[18] L. Winterfeldt, B. Laumert, R. Tano, J.F. Geneau, R. Blasi, G. Hagemann, Redesign of the Vulcain 2 nozzle extension, AIAA Paper 2005-4536, July 2005.